

A Precision Measurement of Inclusive g_2^n and d_2^n with SoLID on a Polarized ^3He Target at 8.8 and 11 GeV

(A Run-Group Proposal Submitted to PAC 48)

Whitney R. Armstrong, Sylvester J. Joosten, Chao Peng¹
Argonne National Laboratory, Argonne, IL

Ye Tian^{1 2}, Weizhi Xiong
Syracuse University, Syracuse, NY

Zhiwen Zhao
Duke University, Durham, NC

E12-10-006 collaboration*, E12-11-007 collaboration[†], and the SoLID Collaboration

¹Spokesperson

²Contact person: tianye@jlab.org

*The collaboration list can be found at https://webhome.phy.duke.edu/~mep/pac38/update/E12-10-006_Collaboration.pdf

[†]The collaboration list can be found at https://www.jlab.org/exp_prog/12GEV_EXP/E1211007.html

Abstract

We propose a precision measurement of neutron spin structure function $g_2(x, Q^2)$, running in parallel with E12-10-006 and E12-11-007, which has been approved by PAC35 and PAC37 separately. In the proposed experiment, high statistics data will be collected within a large kinematic coverage of Bjorken scaling $x > 0.1$ and four momentum transfer $1.5 < Q^2 < 10 \text{ GeV}^2$ from inclusive scatterings of longitudinally polarized electrons off transversely and longitudinally polarized ^3He targets, at incident beam energies of 11 GeV and 8.8 GeV. In addition to mapping out the x and Q^2 evolution of g_2 , we will also extract the moment $d_2(Q^2)$ with $1.5 < Q^2 < 6.5 \text{ GeV}^2$, which is connected to the quark-gluon correlations within the nucleon. This quantity is one of the cleanest observables that can be used to test the theoretical calculations from Lattice QCD and various nucleon structure models.

Contents

1	Physics Motivation	1
1.1	The Spin Structure Functions g_2	1
1.2	The Matrix Element d_2	2
1.3	Burkhardt–Cottingham Sum rule	2
1.4	Current Status of $g_2(x, Q^2)$ and $d_2(Q^2)$ Measurements	3
2	The Proposed Experiment	6
2.1	Polarized ^3He Target	6
2.2	SoLID-SIDIS Detectors	6
2.3	Trigger Design and Rates Estimation	7
3	Extraction of structure functions	9
3.1	Cross Section Differences	9
3.2	Radiative Corrections	10
3.3	Nuclear Effects	11
3.4	Systematic Uncertainties	12
4	Expected Results—Projections	14
4.1	Kinematic Coverage	14
4.2	g_2^n and d_2^n Projections	15
5	Summary	19

List of Figures

1.1	d_2^n versus Q^2 , present world data are shown from SLAC E155x [1], JLab E99–117 [2], JLab RSS [3] and JLab E01–012 [4]. Also shown are various theoretical calculations, including a QCD sum rule approach [5, 6], a chiral soliton model [7] and a bag model [8]. Additionally, a lattice QCD [9] calculation is shown. The elastic contribution to d_2^n is drawn by the dashed curve, evaluated using the CN moments. Figure reference [10].	4
1.2	The status for the observable d_2 of recent neutron [11] and proton [12] measurements with their systematic uncertainties (displayed in the lower bands). Previous world data for $d_2(x, Q^2)$ of proton(neutron) measurements are shown with filled(open) symbols from SLAC [13], E99-117 and E155x [14], and RSS [3] experiments. The dashed (dotted) lines show the elastic contribution for the proton (neutron). The panel on the right shows proton model calculations from QCD sum rules [5, 6], the bag model [15], the Center-of-Mass (CM) bag model [8], the chiral soliton model [7], and light-cone wave functions (LCWF) [16]. The models are calculated at $Q^2 = 5 \text{ GeV}^2$, except the sum rules and LCWF, which were evaluated at $Q^2 = 1 \text{ GeV}^2$. Figure reference [12].	5
2.1	The SoLID-SIDIS layout with CLEO magnet. The large-angle electron measurement is performed by the GEM trackers 1-4, large-angle SPD, and large-angle EC. The forward-angle detection system, for electrons and hadrons, is composed of all GEM trackers, LGC, HGC, MRPC, the forward-angle SPD, and the forward-angle EC.	7
3.1	The kinematic factor C_{\perp}/C_{\parallel} for g_2 extraction from cross section differences. . . .	10
3.2	The kinematic factor C_{\perp}/C_{\parallel} for g_1 extraction from cross section differences. . . .	11
4.1	x versus Q^2 distribution for simulated inclusive events. Left: with 11 GeV incident beam. Right: with 8.8 GeV incident beam	15
4.2	Expected $x^2 g_2^n$ versus x distribution at 8.8 GeV beam energy. Each subplot depicts the projections within a selected Q^2 bin. Error bars are statistical only, while systematic errors are shown with the gray shaded region. The black filled circles present the $x^2 g_2^n$ projection with a prescale factor “10”, and the red open dots, shifted horizontally, represent the projection with a prescale factor “2” (count for the random coincident trigger events).	16
4.3	Expected $x^2 g_2^n$ versus x distribution at 11 GeV beam energy. Each subplot depicts the projections within a selected Q^2 bin. Error bars are statistical only, while systematic errors are shown with the gray shaded region. The black filled circles present the $x^2 g_2^n$ projection with a prescale factor “10”, and the red open dots, shifted horizontally, represent the projection with a prescale factor “2” (count for the random coincident trigger events).	17

4.4 Expected results of d_2^n with trigger prescale factor “10” are shown by red points at 11 GeV and blue points at 8.8 GeV, respectively. The statistical and systematic uncertainties added in quadrature are shown as the error bars. The world data E155x [13], E99-117 and E155x [14], RSS [3], E06-014 [11], E01-012 [4], and the calculation of lattice QCD [9] at $Q^2 = 5 \text{ GeV}^2$ are presented with black open symbols, while the projections of E12-06-121 are marked as black solid dots. For a better visualization, the 8.8 GeV projections and E12-06-121 projections are manually shifted along the vertical axis, and the world data E155x, RSS+pQCD, and E99-117+E155x are shifted horizontally around $Q^2 = 5 \text{ GeV}^2$ 18

Chapter 1

Physics Motivation

Since the late 1970s, polarized lepton beams scattering off polarized nucleons and light nuclear target (i.e., D_2 and ^3He) has been actively studied theoretically and experimentally, providing us important tools in understanding the spin structure of nucleons. In particular, deep inelastic scattering (DIS) has served as one of the major experimental tools to study the quark and gluon structure of the nucleon.

1.1 The Spin Structure Functions g_2

For inclusive polarized electron scattering off a polarized nucleon target, with the one photon exchange approximation, the cross section depends on four structure functions $F_1(x, Q^2)$, $F_2(x, Q^2)$, $g_1(x, Q^2)$, and $g_2(x, Q^2)$, which can be written as bellows,

$$\frac{d^2\sigma}{dE' d\Omega} = \sigma_{Mott} \left[\frac{1}{\nu} F_2(x, Q^2) + \frac{2}{M} F_1(x, Q^2) \tan^2 \frac{\theta}{2} + \gamma g_1(x, Q^2) + \delta g_2(x, Q^2) \right], \quad (1.1)$$

where $F_1(x, Q^2)$ and $F_2(x, Q^2)$ are the spin averaged structure functions and $g_1(x, Q^2)$ and $g_2(x, Q^2)$ are the spin dependent structure functions. In the naive quark parton model, $F_1(x, Q^2)$ or $F_2(x, Q^2)$ gives the quark momentum distribution and the longitudinal polarized structure function $g_1(x, Q^2)$ probes the quark spin distribution [17].

The transverse polarized structure function $g_2(x, Q^2)$ is zero in the naive parton models. However, if one allows the constituent quarks to have an intrinsic transverse momentum in the nucleon, the value of $g_2(x, Q^2)$ can be non-zero and it carries the information of the quark–gluon interaction inside the nucleon. By neglecting quark masses, $g_2(x, Q^2)$ can be decoded by a leading twist–2 term and a higher twist term as follows:

$$g_2(x, Q^2) = g_2^{WW}(x, Q^2) + \bar{g}_2(x, Q^2), \quad (1.2)$$

where twist–2 term g_2^{WW} was derived by Wandzura and Wilczek [18] and it only depends on well-measured g_1 [19, 20], as is shown in Eq. (1.3).

$$g_2^{WW}(x, Q^2) = -g_1(x, Q^2) + \int_x^1 \frac{g_1(y, Q^2)}{y} dy, \quad (1.3)$$

The higher–twist contribution to $g_2(x, Q^2)$ is given by $\bar{g}_2(x, Q^2)$, which can be further expressed in terms of the transverse polarization density $h_T(x, Q^2)$ function [8] and the quark–gluon correlation function $\xi(y, Q^2)$, as is shown in Eq. (1.4)

$$\bar{g}_2(x, Q^2) = - \int_x^1 \frac{\partial}{\partial y} \left(\frac{m}{M} h_T(y, Q^2) + \xi(y, Q^2) \right) \frac{dy}{y}. \quad (1.4)$$

The quantity $y = (E - E')/E$ is the fractional energy transferred to the target. The $h_T(x, Q^2)$ contribution to \bar{g}_2 is suppressed by the ratio of the quark to nucleon masses $\frac{m}{M}$ [8] and thus it is small for up and down quarks and will be negligible in DIS region. As the result, the twist-3 part (ξ) arises from quark-gluon correlation can be accessed from the data of this proposal cleanly.

In summary, the $g_2(x, Q^2)$ structure function is of particular interest because it probes transversely and also longitudinally polarized parton distributions inside the nucleon. Furthermore, $g_2(x, Q^2)$ structure function uniquely measures the twist-3 contributions. The main purpose of this proposal is to extract the transverse spin structure function $g_2^n(x, Q^2)$ from ^3He data. More details are presented in Chapter 3.

1.2 The Matrix Element d_2

The quantity $d_2(Q^2)$, x^2 moment of $\bar{g}_2(x, Q^2)$, measures deviations of $g_2(x, Q^2)$ from the twist-2 term g_2^{WW} . At large Q^2 , where the operator product expansion (OPE) [21] becomes valid, one can access the twist-3 effects of quark-gluon correlations via the third moment of a linear combination of $g_1(x, Q^2)$ and $g_2(x, Q^2)$ presented as

$$d_2(Q^2) = 3 \int_0^1 x^2 [g_2(x, Q^2) - g_2^{WW}(x, Q^2)] dx = \int_0^1 x^2 [2g_1(x, Q^2) + 3g_2(x, Q^2)] dx. \quad (1.5)$$

Due to the x^2 -weighting, the x^2 moments, $d_2(Q^2)$, is particularly sensitive to the large- x behavior of \bar{g}_2 and provides us a clean way to access twist-3 contribution.

Theoretically, there are two major interpretations of $d_2(Q^2)$ in the literature. The first one connects it with color electromagnetic fields induced in a transversely polarized nucleon probed by a virtual photon [22]. The second one shows that the matrix element connected to d_2 , which represents an average color Lorentz force acting on the struck quark due to the remnant di-quark system at the instant, and it is struck by the virtual photon [23]. Beside this, the quantity d_2 is calculable from Lattice QCD [24], and it is one of the few quantities that both Lattice QCD and experiments can have high precision.

Experimentally, the x^2 weighting makes the high x contribution more important, while the low x extrapolation less important. It thus makes JLab the most suitable facility for this measurement.

Furthermore, the quantity d_2 also appears in the first moment of g_1 . It is expressed in terms of a twist expansion with a power series in $\frac{1}{Q^2}$ [25]:

$$\Gamma_1(Q^2) = 3 \int_0^1 g_1(x, Q^2) dx = \frac{1}{2} a_0 + \frac{M^2}{9Q^2} (a_2 + 4d_2 + 4f_2) + \mathcal{O}\left(\frac{M^4}{Q^4}\right), \quad (1.6)$$

where $a_{0,2}$, d_2 , f_2 are the reduced matrix elements of the twist-2, twist-3, and twist-4 components, respectively, and M is the nucleon mass. The quantity f_2 is also sensitive to quark-gluon correlations [26], but it cannot be measured directly. It can be extracted from g_1 data by utilizing a twist expansion of Γ_1 by first subtracting a_0 from Γ_1 and then fitting the result as a function of $\frac{1}{Q^2}$.

1.3 Burkhardt-Cottingham Sum rule

The spin structure function $g_2(x, Q^2)$ is expected to obey the Burkhardt-Cottingham sum rule [27, 28] (BC sum rule), which reveals the integral of g_2 on the whole x region. From the BC sum rule, the first moment of g_2 is expected to be zero at all Q^2 (Eq. (1.7)). Therefore, the

BC sum rule indicates that the elastic and the inelastic contributions to the first moment of g_2 should cancel for any value of Q^2 .

$$\Gamma_2(Q^2) = \int_0^1 g_2(x, Q^2) dx = 0 \quad (1.7)$$

In real world experiments, it is impractical to fully cover the whole integral region ($0 < x < 1$). In order to test the BC sum rule, one feasible way is to use the elastic form factors for the elastic contribution and assume $g_2 = g_2^{WW}$ in the $x \rightarrow 0$ region. Therefore, the BC sum rule's validity depends on the convergence properties of the integral and assumes that g_2 is analytic in the $x \rightarrow 0$ limit. This proposal will extract $g_2^n(x, Q^2)$ within $x > 0.1$. Such experimental data provide an opportunity to further explore the large x contributions to this sum rule for the neutron.

1.4 Current Status of $g_2(x, Q^2)$ and $d_2(Q^2)$ Measurements

The dedicated measurements of g_2 were carried at several laboratories including SLAC [13, 1], DESY [29] and Jefferson Lab (JLab) [30, 31, 2, 32, 14, 3, 12, 33]. The corresponding detailed target information, measured observables, and kinematic coverage are listed in Tab. 1.1. At JLab, g_2 and its moments have been extensively measured for the neutron with a polarized ^3He target for Q^2 up to 4.8 GeV^2 . Even though the SLAC data (E155 [13] and E155x [1]) cover a wider kinematic range $0.02 \leq x \leq 0.8$ and $0.7 \leq Q^2 \leq 20$, but with their data structure the twist-3 matrix element d_2^n can be extracted at average $\langle Q^2 \rangle = 5 \text{ GeV}^2$ only. The ongoing Hall C g_2^n - d_2^n experiment E12-06-121 will measure g_2^n over the kinematic region $0.2 < x < 0.95$ and $2.5 < Q^2 < 7 \text{ GeV}^2$ and evaluate the twist-3 matrix element d_2^n . Partial kinematic coverage of this proposed measurement will overlap with Hall C E12-06-121 experiment, but the cross sections of those two experiments are measured by completely independent apparatuses, which will be used to extract g_2 and evaluate the d_2^n . Together, these two measurements would provide a better understanding of the twist-3 matrix element $d_2^n(Q^2)$, and the associated quark-gluon correlations within the nucleon.

Table 1.1: Summary of Previous Measurements of g_2 , d_2 and Γ_2

Target	Observable	x/W value	Q^2 value GeV ²	Lab/experiment
NH ₃ , ⁶ LiD	$g_2^p, g_2^d,$ d_2^p, d_2^d	$0.02 \leq x \leq 0.8$	$1 \leq Q^2 \leq 30$	SLAC E155 [13]
NH ₃ , ⁶ LiD	$g_2^p, g_2^d,$	$0.02 \leq x \leq 0.8$	$0.7 \leq Q^2 \leq 20$	SLAC E155X [1]
H ₂	g_2^p	$0.04 \leq x \leq 0.9$	$0.18 \leq Q^2 \leq 20$	DESY HERMES [29]
³ He	g_2^n, d_2^n, Γ_2^n	$0.5 \leq W \leq 2.5 \text{ GeV}$	$0.1 \leq Q^2 \leq 0.9$	JLAB E94-010 [30]
³ He	g_2^n	$x = 0.2$	$0.57 \leq Q^2 \leq 1.34$	JLAB E97-103 [31]
³ He	g_2^n, d_2^n	$x = 0.33, 0.47, 0.6$	2.7, 3.5, 4.8	JLAB E99-117 [2]
³ He	g_2^n	$x < 0.1$	$0.035 \leq Q^2 \leq 0.24$	JLAB E97-110 [32]
³ He	g_2^n, d_2^n	$0.25 \leq x \leq 0.9$	3.21, 4.32	JLAB E06-014 [14]
³ He	g_2^n, d_2^n	$0.55 \leq x \leq 0.9$	$0.7 \leq Q^2 \leq 4.0$	JLAB E01-012 [34]
NH ₃ , ND ₃	g_2^p, d_2^p, d_2^n	$1.085 \leq W \leq 1.91 \text{ GeV}$	~ 1.3	JLab E01-006 [3]
NH ₃	g_2^p, d_2^p	$0.3 \leq x \leq 0.8$	$2.5 \leq Q^2 \leq 6.5$	JLab E03-109 [12]
NH ₃	g_2^p	$1.07 < W < 2.09 \text{ GeV}$	$0.02 \leq Q^2 \leq 0.4$	JLab E08-027 [33]

The experimental and theoretical results for twist-3 matrix element d_2 of neutron and proton are shown in Fig. 1.1 and 1.2. At $Q^2 = 5 \text{ GeV}^2$, the lattice prediction on the neutron

matrix element d_2^n [9] gives a negative value but close to zero, which is consistent with the predictions of bag and chiral Soliton model at the same Q^2 , while the prior experimental data differ with those calculations by roughly two standard deviations. However for proton d_2^p , the measurements have a better agreement with the Lattice and model calculations at the same large Q^2 region ($Q^2 = 5 \text{ GeV}^2$), which is illustrated by the data in Fig. 1.2. Interestingly, at $2.7 \text{ GeV}^2 < Q^2 < 5 \text{ GeV}^2$, where a theoretical interpretation in terms of twist-3 is cleaner, the E06-014 neutron data (Hall A) shows a sizable negative value of d_2 at $Q^2 \sim 3 \text{ GeV}^2$, which is equal to that of the recent SANE proton data (Hall C), as is shown in Fig 1.2. The world proton and neutron data in Fig. 1.2 and Fig. 1.1 both indicate a non-trivial scale dependence of d_2 .

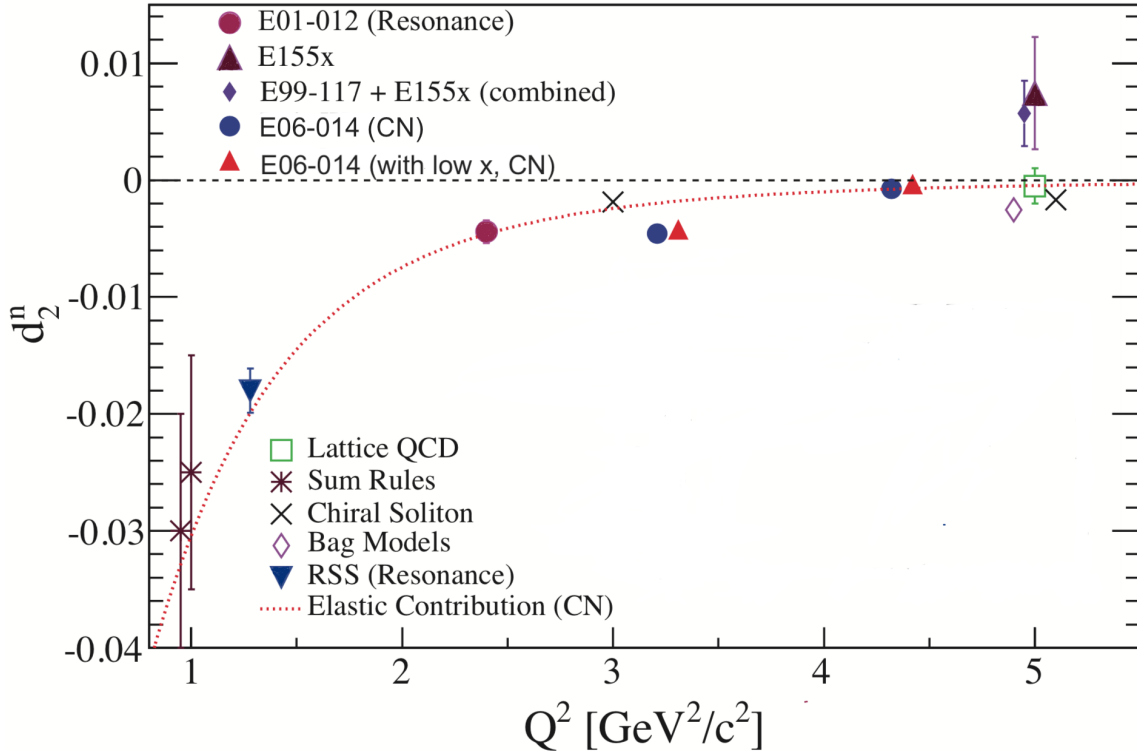


Figure 1.1: d_2^n versus Q^2 , present world data are shown from SLAC E155x [1], JLab E99-117 [2], JLab RSS [3] and JLab E01-012 [4]. Also shown are various theoretical calculations, including a QCD sum rule approach [5, 6], a chiral soliton model [7] and a bag model [8]. Additionally, a lattice QCD [9] calculation is shown. The elastic contribution to d_2^n is drawn by the dashed curve, evaluated using the CN moments. Figure reference [10].

The existing proton data on $d_2(Q^2)$ also exhibit an interesting trend over Q^2 . At $Q^2 \sim 1 \text{ GeV}^2$, the RSS experiment reported a sizeable positive value, while in the higher Q^2 region ($Q^2 = 2.8, 4.3 \text{ GeV}^2$), negative values were observed from the SANE data, though they are still consistent with zero considering the systematic uncertainties. Finally at $Q^2 \sim 5 \text{ GeV}^2$, proton d_2 turns back to positive, as reported by SLAC 155X. However, the data precision at large Q^2 is insufficient to discriminate between the QCD based predictions, as shown in Fig. 1.2.

Therefore, precision measurements at 12 GeV Jefferson Lab with transversely polarized neutron targets (SoLID E12-10-006 [35]) and proton (SoLID E12-11-108 [36]) experiments are crucial to investigate the $d_2(Q^2)$ behavior. Furthermore, the modern lattice QCD calculations of d_2 , performed at the physical pion mass without chiral extrapolation, including disconnected diagrams without the quenched approximation [24] are sorely needed for a complete understanding of the world data.

In summary, we need to accumulate sufficient and precise data on $g_2(x, Q^2)$ and $d_2(Q^2)$

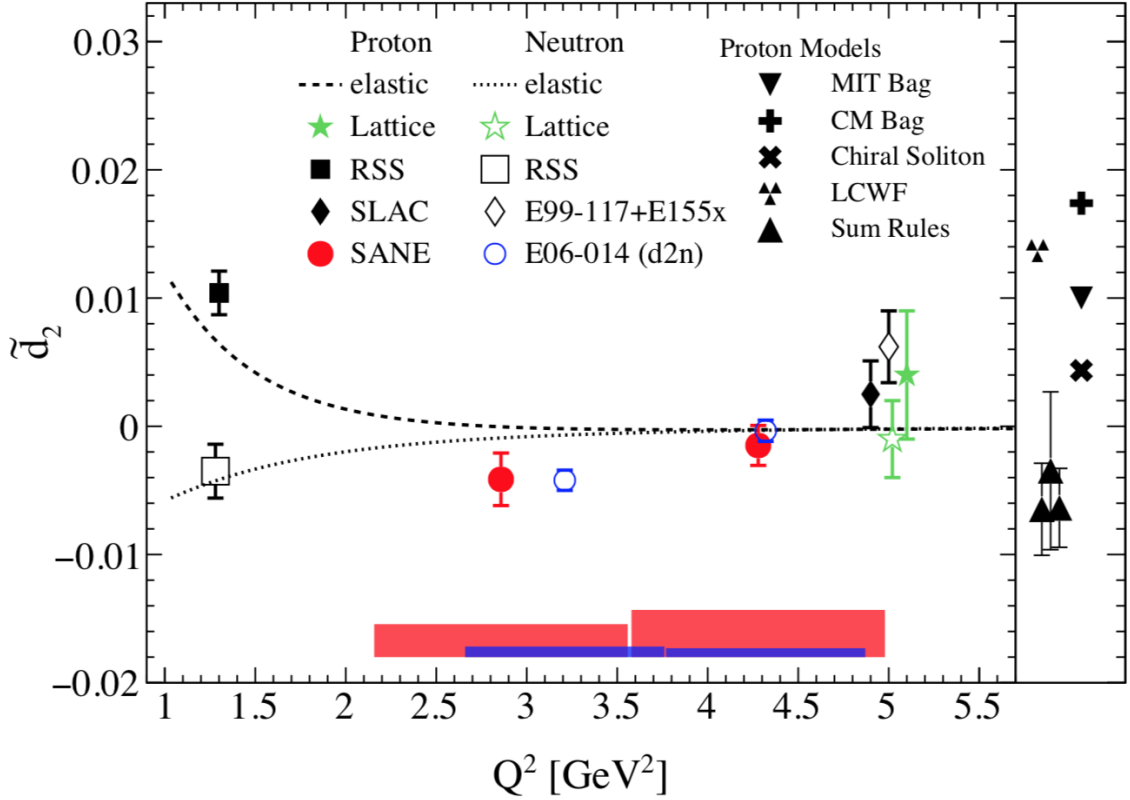


Figure 1.2: The status for the observable d_2 of recent neutron [11] and proton [12] measurements with their systematic uncertainties (displayed in the lower bands). Previous world data for $d_2(x, Q^2)$ of proton(neutron) measurements are shown with filled(open) symbols from SLAC [13], E99-117 and E155x [14], and RSS [3] experiments. The dashed (dotted) lines show the elastic contribution for the proton (neutron). The panel on the right shows proton model calculations from QCD sum rules [5, 6], the bag model [15], the Center-of-Mass (CM) bag model [8], the chiral soliton model [7], and light-cone wave functions (LCWF) [16]. The models are calculated at $Q^2 = 5$ GeV², except the sum rules and LCWF, which were evaluated at $Q^2 = 1$ GeV². Figure reference [12].

to map out the transition between a partonic description to a hadronic description of the nucleon, and poised to push the QCD-based calculation forward. Thus, we propose to analyze the E12-10-006 and E12-11-007 data to extract the spin structure function $g_2^n(x, Q^2)$ with high statistics and large kinematic coverage for Bjorken scaling $x > 0.1$ and four momentum transfer $1.5 < Q^2 < 10$ GeV². The data will allow us to evaluate $d_2^n(Q^2)$ within $1.5 < Q^2 < 6.5$ GeV².

Chapter 2

The Proposed Experiment

We propose to extract the spin-dependent structure function $g_2(x, Q^2)$ at momentum transfer $1.5 < Q^2 < 10 \text{ GeV}^2$ and Bjorken scaling $x > 0.1$ from the inclusive measurement of longitudinally polarized electrons scattering off a transversely polarized ^3He target. The proposed measurement will run in parallel with E12-10-006, which has been approved by PAC35. The interested kinematic region will be covered with the Solenoidal Large Intensity Device (SoLID) in SIDIS-configuration and the two beam energies at 8.8 GeV and 11 GeV.

2.1 Polarized ^3He Target

The experiment will utilize the same target system proposed for E12-10-006 [35]. It is a high-pressure (~ 10 atm) polarized ^3He target, serving as the effective neutron target. The ^3He gas stored in a 40-cm-long cell is polarized by the spin-exchange with optical pumped Rb-K alkali atoms. Three sets of Helmholtz coils encompassing the target cell will hold the polarization direction. With this target system operated at an average of 60% in-beam polarization, we expect a full polarized luminosity of $10^{36} \text{ cm}^{-2} \cdot \text{s}^{-1}$ for a beam current at $15 \mu\text{A}$. Such a target polarization level has already been achieved in the previous experiment E06-010 [37].

2.2 SoLID-SIDIS Detectors

As shown in Fig. 2.1, the detector package in the SIDIS configuration is composed of six Gas Electron Multiplier (GEM) planes, two Shashlyk sampling Electromagnetic Calorimeters (EC), two Scintillator Pad Detectors (SPD), one Light Gas Cerenkov Detector (LGC), one Heavy Gas Cerenkov Detector (HGC), and one Multi-gap Resistive Plate Chamber (MRPC). The spectrometer is built upon a three-meters-long solenoid magnet with $\int \mathbf{B} d\mathbf{l} = 5 \text{ T} \cdot \text{m}$, named as CLEO-II. For the single electron detection, it provides a full 2π coverage for the azimuthal angle, and 8° - 24° for the polar angle. The momentum acceptance for the electrons is $> 0.8 \text{ GeV}/c$, with a resolution of $\sim 2\%$.

Among these sub-detectors in the SIDIS configuration, the GEM planes provide non-destructive detection of charged particles with an excellent position resolution of about $70 \mu\text{m}$. The positional information from multiple planes together facilitates high-resolution tracking reconstruction for the charged particles. Two ECs, each composed of hexagonal Shashlyk-type modules, destructively measure the energy deposition of particles with a resolution better than $10\%/\sqrt{E}$. The preshower and shower segments of the EC also determine energy deposit profiles that can identify electrons from hadrons. The SPD will be installed in front of each EC detector, mainly serving as veto detectors for photons to suppress the calorimeter-based trigger rates. The large-angle SPD also measures the time-of-flight (TOF) for identification between charged

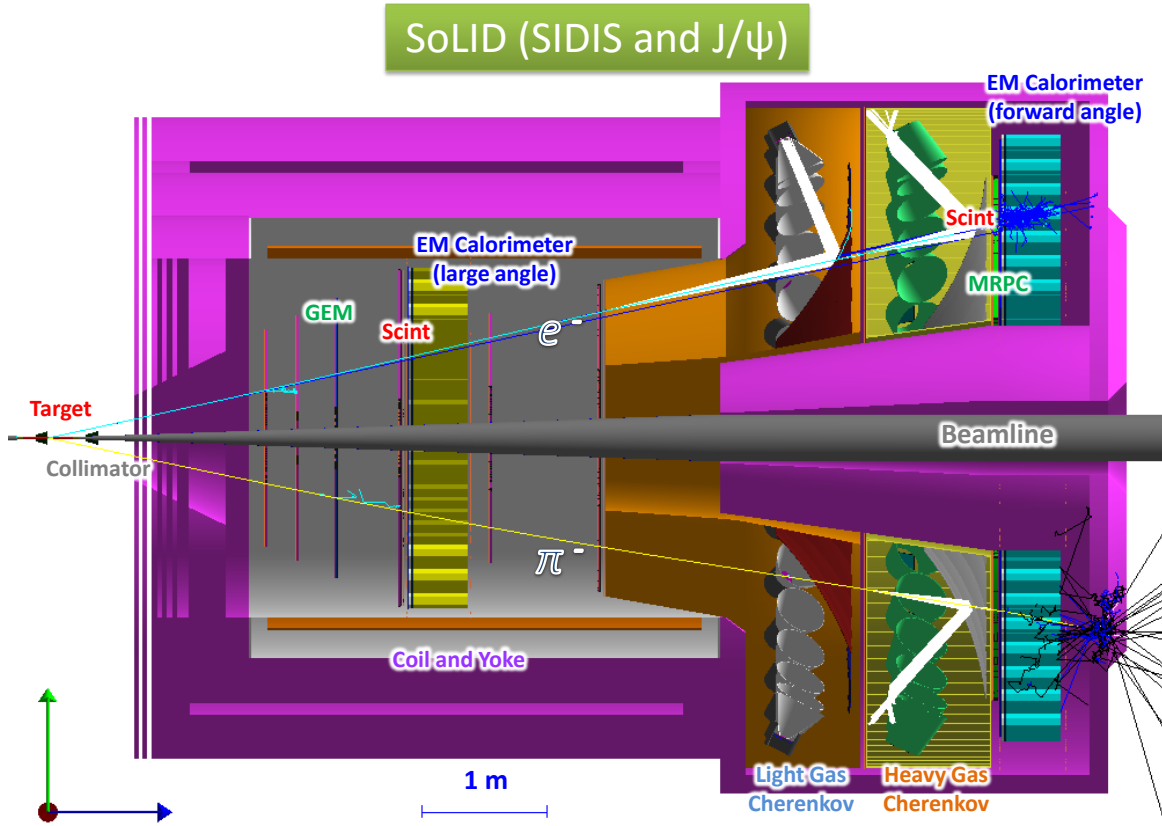


Figure 2.1: The SoLID-SIDIS layout with CLEO magnet. The large-angle electron measurement is performed by the GEM trackers 1-4, large-angle SPD, and large-angle EC. The forward-angle detection system, for electrons and hadrons, is composed of all GEM trackers, LGC, HGC, MRPC, the forward-angle SPD, and the forward-angle EC.

particles, while the MRPC, located in front of the forward-angle calorimeter, provides precise TOF information for the forward angle detection. In addition, the LGC and HGC detectors can separate the charged particles for electrons/pions and pions/kaons in the forward-angle region, respectively.

2.3 Trigger Design and Rates Estimation

Estimated single electron trigger rates from 12-10-006 run group [35, 38, 39] are listed in Tab. 2.1. The total rates with hadron backgrounds for the SIDIS- ^3He experiment is about 128.3 kHz. Considering the estimated total coincident trigger is ~ 85 kHz for the experiments in E12-10-006 run group, and the designed trigger limit of the data acquisition system is better than 100 kHz, a capacity of about 15 kHz trigger rate is left for the single electron triggers. Therefore, the proposed experiment will require exclusive single electron triggers with a prescale factor of “10”.

The single electron trigger at the forward angle (FA) detectors will be formed by a coincidence of the gas Cherenkov detector, the EM calorimeter, and the scintillator paddle detector (SPD). At large angle, this trigger is provided by the EM calorimeter at a threshold of about 3 GeV coincident with SPD. The DIS e^- events are generated based on the CTEQ parton distribution functions (PDF) to estimate the trigger rates. For background rates estimation, hadron events are generated with the “bggen” event generator from 12-10-006 run group. Single π^- cross section calculated from the “bggen” generator agree with the MARATHON data [40] at

Table 2.1: Estimate of trigger rates

Single e^- trigger	Target cell rates (kHz)	Target upstream window rates (kHz)	Target downstream window rate (kHz)
FA e^-	59	1.15	1.8
FA hadron background	28.6	3.9	5.6
LA e^-	4.1	3.6	2.6
LA hadron background	7.7	6.5	3.8
Total single e^- trigger rate	128.3		

30% level. Furthermore, the cross section of π^0 , the main source of the backgrounds, calculated from the “bggen” generator is consistent with that extracted from DVCS experiment [41] within 20 – 30%. As the result, we expect about 20 – 30% fluctuation for the total trigger rates listed in Tab. 2.1.

The coincident trigger ~ 85 kHz, estimated from the experiments in E12-10-006 run group, includes about 54 kHz of random coincident trigger rate. These are indeed triggered by single electrons and random coincidence from hadron background, and thus can be reused for this proposed experiment. The random trigger rate, added upon the prescaled 15 kHz single electron trigger rate, allow us to achieve a 69 kHz rates for the inclusive electrons, which is equivalent to a prescale factor of “2” on the simulated yield. In practice, reusing these trigger events require a careful study on the possible bias in the random trigger. Since E12-10-006 and E12-11-007 experiments have proposed to set up the event triggers with a prescaled single electron trigger, it ensures that the proposed measurement will have the single electron trigger events to carry out the bias study. In addition, if the eventual DAQ limit can be increased to more than 100 kHz, this proposal will stand to benefit from the extra trigger space.

The yield prescale factors of “2” and “10” are used to test their influences on statistics errors, which are shown in Fig. 4.2, Fig. 4.3.

Chapter 3

Extraction of structure functions

We plan to directly extract the structure functions g_1 and g_2 from the measured cross section differences for the longitudinally polarized electron beam with transversely and longitudinally polarized ^3He targets:

$$\begin{aligned}\Delta\sigma_{\parallel} &= \frac{d^2\sigma^{\downarrow\uparrow}}{d\Omega dE'} - \frac{d^2\sigma^{\uparrow\uparrow}}{d\Omega dE'} \\ &= \frac{4\alpha^2 E'}{M\nu Q^2 E} [(E + E' \cos\theta)g_1(x, Q^2) - 2Mxg_2(x, Q^2)].\end{aligned}\tag{3.1}$$

$$\begin{aligned}\Delta\sigma_{\perp} &= \frac{d^2\sigma^{\downarrow\Rightarrow}}{d\Omega dE'} - \frac{d^2\sigma^{\uparrow\Rightarrow}}{d\Omega dE'} \\ &= \frac{4\alpha^2 E'^2}{M\nu Q^2 E} \sin\theta \cos\phi_{rela} \left[g_1(x, Q^2) + \frac{2E}{\nu} g_2(x, Q^2) \right],\end{aligned}\tag{3.2}$$

where the symbols “ \uparrow ” and “ \uparrow ” illustrate the polarization directions of beam and target, respectively. In this equation, E' represents the scattered electron energy, θ is the scattering angle, and ϕ_{rela} is the azimuthal angle between the scattered electron and the target polarization. The factor $\cos\phi_{rela}$ is maximized when the polarization plane and the scattering plane coincide.

Extraction of neutron structure functions requires further corrections to the nuclear effects for neutrons bound in the ^3He targets. In addition, the complicity of radiative effects for the measured cross section differences necessitate corrections to unfold these quantities to their Born-level (single photon exchange) contribution. These corrections are discussed with more details in the following sections.

3.1 Cross Section Differences

As shown in Equations 3.1 and 3.2, the direct extraction of g_2 requires the cross section differences measured in both the parallel ($\Delta\sigma_{\parallel}$) and perpendicular ($\Delta\sigma_{\perp}$) configurations, in which the target is polarized longitudinally and transversely with respect to the beam direction, respectively. The proposed experiment will measure the perpendicular cross section difference inclusively with the single electron triggers in parallel with E12-10-006. Such data will then be combined with the parallel cross section difference data taken from E12-11-007 [42], which proposed the same beam energies and detector configurations with a longitudinally polarized ^3He target, to extract the neutron structure functions.

In practice, asymmetry measurements are preferred in determination of g_1 and g_2 because major systematic uncertainties associated with the detector performance, luminosity will be cancelled at the first order. The parallel and perpendicular asymmetries can be formed by

combining experimental data from different polarization configurations as

$$\begin{aligned} A_{\parallel} &= \frac{\sigma^{\downarrow\uparrow} - \sigma^{\uparrow\uparrow}}{\sigma^{\downarrow\uparrow} + \sigma^{\uparrow\uparrow}}, \\ A_{\perp} &= \frac{\sigma^{\downarrow\Rightarrow} - \sigma^{\uparrow\Rightarrow}}{\sigma^{\downarrow\Rightarrow} + \sigma^{\uparrow\Rightarrow}}. \end{aligned} \quad (3.3)$$

So $\Delta\sigma_{\parallel,\perp} = 2\sigma_0 A_{\parallel,\perp}$ with σ_0 the unpolarized cross sections, which can be extracted from the sum of charge normalized experimental yields with opposite beam helicity states.

Assuming $\cos\phi_{rela} = 1$, the extraction of g_1 and g_2 can be written as:

$$\begin{aligned} g_1 &= \frac{MQ^2}{4\alpha^2} \frac{\nu E}{(E-\nu)(2E-\nu)} \left[\Delta\sigma_{\parallel} + \tan\frac{\theta}{2} \Delta\sigma_{\perp} \right], \\ g_2 &= \frac{MQ^2}{4\alpha^2} \frac{\nu^2}{2(E-\nu)(2E-\nu)} \left[-\Delta\sigma_{\parallel} + \frac{E + (E-\nu)\cos\theta}{(E-\nu)\sin\theta} \Delta\sigma_{\perp} \right]. \end{aligned} \quad (3.4)$$

The ratio of kinematic factors in front of the cross section differences are depicted in Fig. 3.1 and 3.2. The spin-dependent structure function g_2 heavily relies on the perpendicular cross section difference $\Delta\sigma_{\perp}$ due to the large kinematic factor within the proposed kinematic coverage, while the g_1 is mostly dependent on $\Delta\sigma_{\parallel}$. Therefore, the statistical and systematic uncertainties of g_2 are dominated by those of $\Delta\sigma_{\perp}$.

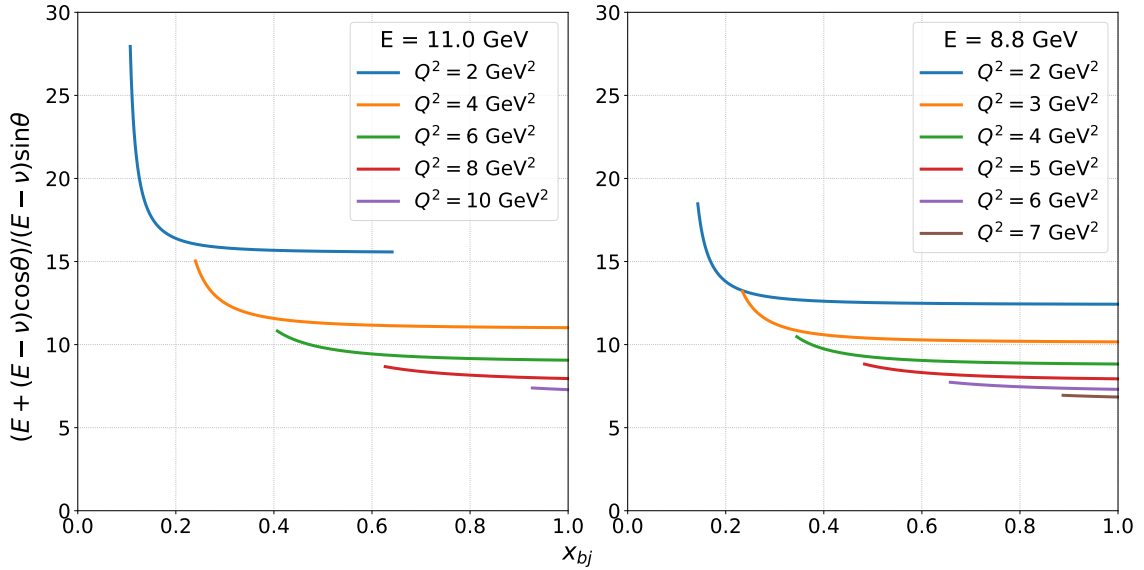


Figure 3.1: The kinematic factor C_{\perp}/C_{\parallel} for g_2 extraction from cross section differences.

3.2 Radiative Corrections

The structure functions are obtained from the inclusive cross section differences at the Born level. However, in the real world the observed cross sections are the “dressed” cross sections convoluted with radiative effects that shift the observed kinematics from these at the interaction vertex. Generally the Born cross sections are unfolded with internal and external radiative corrections. The former includes loop effects and emissions of real or virtual photons, while the latter involves with the ionization energy loss and the Bremsstrahlung process due to scattered electrons passing through matters before or during the detection. Multiple recipes exist for correcting the radiative effects. For the proposed experiment, we will follow the recipes

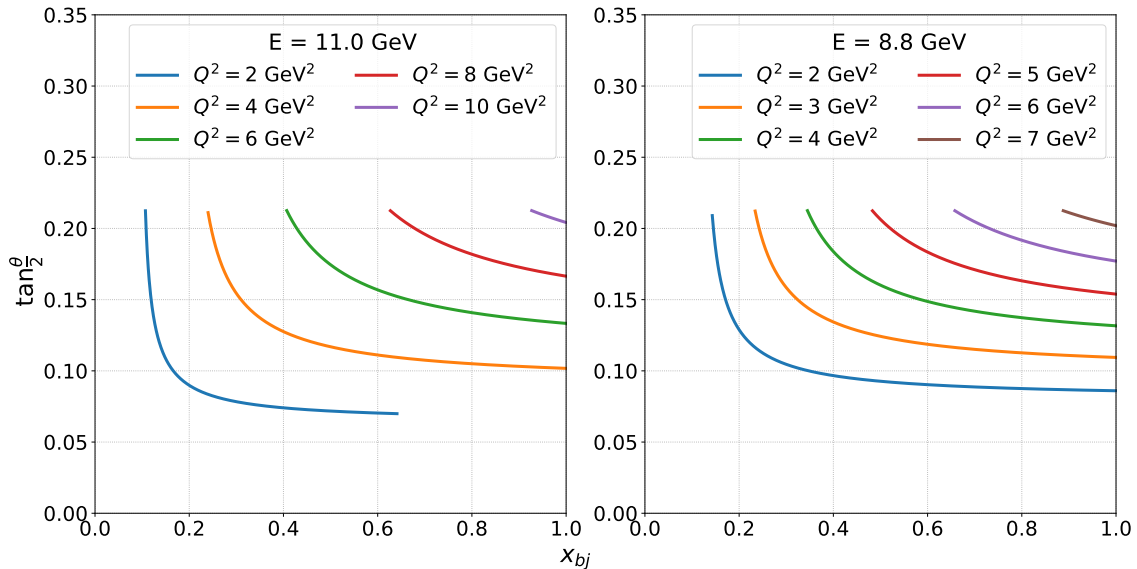


Figure 3.2: The kinematic factor C_{\perp}/C_{\parallel} for g_1 extraction from cross section differences.

developed by Akushevich and Shumeiko [43] to correct the internal radiative effects for the spin dependent cross sections of lepton nucleon scattering.

According to the formula from Tsai [44] with the angle peaking approximation for photon emissions, the internal and external radiative effects are convoluted as

$$\sigma_{rad}(E_s, E_p) = \int \frac{dl}{L} \int_{E_s^{min}}^{E_s} dE'_s \int_{E_p}^{E_p^{max}} dE'_p I(E_s, E'_s, l) \bar{\sigma}(E'_s, E'_p) I(E'_p, E_p, L-l), \quad (3.5)$$

where $\bar{\sigma}$ denotes the cross sections with internal radiative effects, I represents the probability function for the energy losses before (with material thickness l) and after (with material thickness $L-l$) the interaction, and E_s, E_p are the incident beam energy and detected energy of the scattered electron, respectively. Since the cross sections will be measured within a large angle acceptance, it is nearly impractical to unfold the Born cross sections by numerically integrating all the possible electron paths. Therefore, we will utilize a data-driven, iterative procedure to correct the external radiative effects with the Monte-Carlo simulation based on the end-to-end SoLID software framework [45].

During the iterative correction, the initial Born cross sections will be built from the interpolations between the measured points, and modified global fits will be used to constrain the cross sections near the boundaries of kinematic coverage. The ionization and Bremsstrahlung processes, as well as multiple scatterings for electrons passing through the external materials will be simulated with the GEANT4 simulation toolkit [46]. The radiative corrections from the simulation will be applied back to the measured data points, and then update the Born cross sections as the inputs to the simulation. Such a procedure will be repeated until the results from consecutive iterations converge within a satisfied tolerance.

3.3 Nuclear Effects

Polarized ${}^3\text{He}$ often serves as an effective polarized neutron target because its spin at the ground state is mostly carried by the unpaired neutron. The average nucleon polarization in a ${}^3\text{He}$ nucleus is written as $\langle \sigma_z \rangle^n = P_S - \frac{1}{3}(P_D - P_{S'})$. with the space-symmetric S state predominantly contributes to the ground state ($P_S \approx 90\%$) of the polarized ${}^3\text{He}$.

In the effective polarization approximation, the nuclear binding is neglected and $x^2/Q^2 \rightarrow 0$, the polarized ${}^3\text{He}$ structure functions can be formed by a weighted sum of the nucleon structure

functions as

$$g_i^{3He}(x, Q^2) = 2P_i^p g_i^p(x, Q^2) + P_i^n g_i^n(x, Q^2), \quad (3.6)$$

where $i = 1, 2$, and the superscript denotes the nucleus or the nucleon. The weighting factor P_i^N is the effective polarization, which is dominated by the lowest-order contribution $\langle \sigma_z \rangle^N$ and can be calculated from models of ^3He wave functions, such as SS [47] and KPSV [48] spectral functions. However, this approach is not reliable in the nucleon resonance region or at large x , where the Weak Binding Approximation (WBA) is found to be more reliable for correcting the nuclear effects.

In the framework of WBA, the spin dependent structure function of ^3He can be written as [49]:

$$g_i^{3He}(x, Q^2) = \int \frac{dy}{y} \left[2f_{ij}^p(y, \gamma) g_j^p\left(\frac{x}{y}, Q^2\right) + f_{ij}^n(y, \gamma) g_j^n\left(\frac{x}{y}, Q^2\right) \right], \quad (3.7)$$

where $\gamma^2 = 1 + 4M^2x^2/Q^2$, y represents the momentum fraction carried by the nucleons. Here $f(y, \gamma)$ is the nucleon momentum distribution function, which can be calculated with the nuclear spectral functions. In addition, the non-nucleonic degree of freedom and nucleon off-shell corrections can also be incorporated into the framework, though these corrections will introduce additional model-dependent uncertainties. More details can be found in [49].

3.4 Systematic Uncertainties

The systematic uncertainties from cross section measurements based on spectrometers are typically dominated by those associated with the detector acceptance, efficiency, and luminosity. Since SoLID is a large acceptance detector with tracking reconstruction under high intensity circumstances, determining its acceptance and efficiency is expected to be more difficult than that for the existing JLab spectrometers, such as HRS or HMS/SHMS, which could be understood at a level of better than 3%. Thus the estimated uncertainty for SoLID acceptance is given as 5%, and an error of 3% is assigned for the detection efficiency.

The luminosity is composed of beam charge and target density. These two components have already been studied excessively in recent JLab experiments with a polarized electron beam and polarized ^3He targets [32, 37], which gave 2% and 1% uncertainties for the target density and beam charge, respectively. Such experiments also achieved uncertainties of 1.0-2.0% for the beam polarization and 3% for the target polarization. In addition, the correction of dilution effects from the nitrogen gas inside the target cell is expected to contribute a $< 1.0\%$ error.

Raw asymmetry measurement is known to be precise as most of the major systematic contributions are cancelled out at the first order, but the contamination from false asymmetries, such as beam charge asymmetry and pion asymmetry, will introduce absolute asymmetry uncertainties into the results. The beam charge asymmetry at JLab can be controlled at the level of 50 ppm. For the pion charge asymmetries, the SoLID has a pion rejection power of 1 : 50 for $P_e < 2$ GeV and 1 : 150 for $P_e > 2$ GeV. Given the single charged pions rates of 10.3 kHz from ‘‘bggen’’, which are about one sixth of the single electron rates, and a maximum of pion asymmetry at 15% [50], the pion contamination is less than 5×10^{-4} .

Scattering electrons from the target cell or the nitrogen gas inside the cell will introduce backgrounds to the yields. The major background contribution from the cell can be rejected at the first order by cutting off the windows with reconstructed vertex z position, while the higher order effects and the nitrogen gas contribution will be corrected with data taken from a reference nitrogen cell. The asymmetry dilution effect from these unpolarized materials is typically less than 10% with the JLab polarized ^3He target, and thus an error of $< 1\%$ is assigned for the corresponding corrections. For cross sections, background subtractions will be

performed with the reference data, and we assume a 3% error accounted for the residual higher order effects and imperfect yields normalization between production runs and reference runs.

In addition, measured experimental cross section (difference) for polarized ^3He targets need to be unfolded to the neutron cross section (difference) at Born level. Since the nuclear corrections are nontrivial within our kinematic coverage, and it is likely to introduce model-dependent uncertainties as discussed in the above section, we have given a conservative estimate, 5%, for this item. The uncertainty of radiative correction (3%) is obtained from the study for experiment E97-110 [32], which had applied an iterative radiative correction procedure similar to the proposed method discussed in Section 3.2.

All the above-mentioned uncertainties are summarized in Tab. 3.1. The total uncertainties propagated to g_2 and d_2 are also listed. Please refer to Figure 4.2 and Figure 4.3 for statistical uncertainties of g_2 , which are not shown below in numbers due to significant variations over the kinematic coverage.

Table 3.1: Estimate of uncertainties for the proposed experiment.

Source	Systematic Uncertainty
Cross Sections	
Detector acceptance	5.0%
Detector efficiencies	3.0%
Target density	2.0%
Beam charge	1.0%
Background subtraction	3.0%
Asymmetries	
Dilution effects	$< 1.0\%$
Beam polarization	$< 2.0\%$
Target polarization	3.0%
Charge asymmetry	$< 10^{-4}$
Pion asymmetry	$< 5 \times 10^{-4}$
Unfolding Procedure	
Nuclear corrections	$\sim 5.0\%$
Radiative corrections	$\sim 3.0\%$
Physics Results	
Cross sections	$< 10.0\%$
g_2 syst.	$\sim 10^{-3}-10^{-4}$
d_2 stat.	$\sim 3 \times 10^{-4}$
d_2 syst. (11 GeV)	$\sim 5 \times 10^{-4}$
d_2 syst. (8.8 GeV)	$\sim 8 \times 10^{-4}$

Chapter 4

Expected Results—Projections

The expected yields and corresponding statistical errors estimated in this section are based on a full simulation of inclusive inelastic scattering with the SoLID SIDIS acceptance folded in. The simulation events presented in this proposal are generated by SoLID `inclusive_electron_e` event generator, which includes quasi-elastic, resonance and DIS processes. For $W < 3$ GeV region, the generator generate events based on the Peter Bosted fit, while for $W > 3$ GeV, the world PDF [51] fits are applied.

4.1 Kinematic Coverage

The transverse polarized structure function g_2^n can be extracted from the cross section differences with kinematic variables x and Q^2 . The range of each kinematic variable is determined by the kinematic nature of the data, and the bin size is needed to be chosen as fine as possible to address the structure of the g_2 ; meanwhile we also need to minimize the statistical uncertainties to guarantee enough statistics in each kinematic bin. One possible binning solution is listed in Tab. 4.1 and 4.2.

We propose to measure inclusive electron scatterings during the SIDIS experiments E12–10–006 [35] and E12–11–007 [42] with a beam current of $15 \mu\text{A}$ at incident beam energies of 11 GeV and 8.8 GeV on the transversely and longitudinally polarized ^3He targets. Thus, this run group proposal does not require any additional beam time. The requested beam time from experiment E12–10–006 and E12–11–007 is listed in Tab. 4.3.

By considering the acceptance and detector efficiency from the SoLID-SIDIS experiment E12–10–006, the kinematic coverage of the proposed inclusive events is illustrated in Fig. 4.1 (without any W cut). Lines on these plots show the boundaries of the kinematic region of interest.

Table 4.1: x_{jb} and Q^2 binning at 8.8 GeV beam energy.

Variable	Lower limit	Upper limit	Number of bins	Bin size
x_{jb}	0.1	1	9	0.1
Q^2, GeV^2	1.5	7.5	30	0.2

Table 4.2: x_{jb} and Q^2 binning at 11 GeV beam energy.

Variable	Lower limit	Upper limit	Number of bins	Bin size
x_{jb}	0.1	1	9	0.1
Q^2, GeV^2	2.0	10.0	40	0.2

Table 4.3: Proposed Beam time from SoLID SIDIS proposal E12-10-006 and E12-11-007

Measurements	Time (hours)	Time (days)
Production on transversely polarized ^3He with 11 GeV beam	1152	48
Production on transversely polarized ^3He with 8.8 GeV beam	504	21
Production on longitudinally polarized ^3He with 11 GeV beam	538	22.5
Production on longitudinally polarized ^3He with 8.8 GeV beam	228	9.5

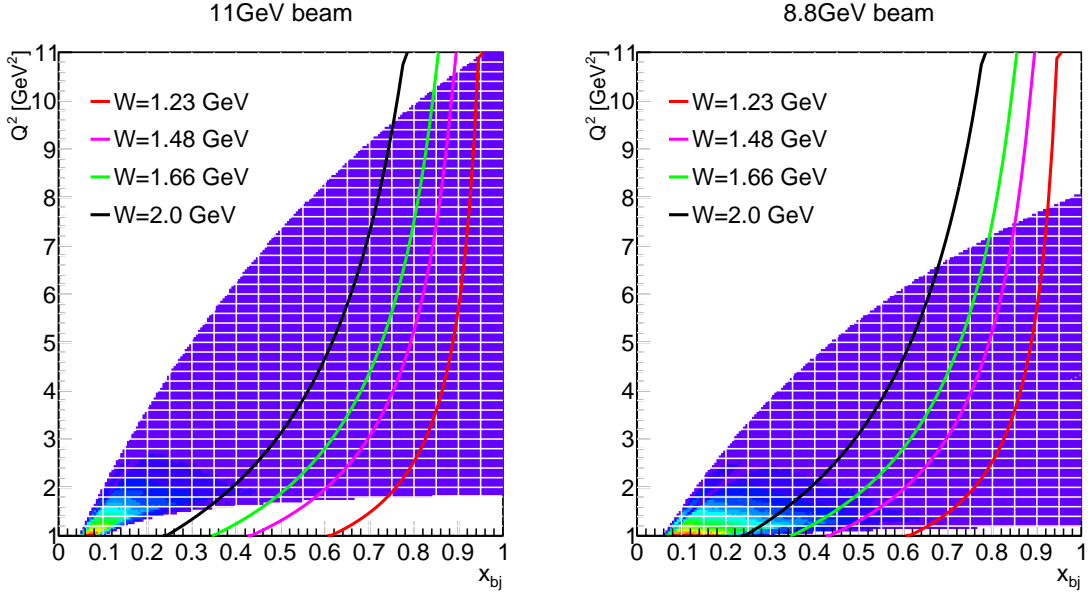


Figure 4.1: x versus Q^2 distribution for simulated inclusive events. Left: with 11 GeV incident beam. Right: with 8.8 GeV incident beam

4.2 g_2^n and d_2^n Projections

The simulated event yields, with the polarized luminosity of $10^{36} \text{ cm}^{-2} \cdot \text{s}^{-1}$ and the requested production time (as shown in the Tab. 4.3), are generated to estimate the statistical uncertainties of the proposed observable g_2^n . Meanwhile, a single electron prescale trigger factor of “10” is included in the simulated yields to satisfy the DAQ limit 100 kHz of the E12-10-006 and E12-11-007 experiments.

The twist-2 term g_2^{WW} (Eq. (1.3)), only depends on well-measured g_1 , is used to present the expected g_2 precision. The polarized structure function g_1^n obtained from the SLAC E155x fits [52] and the unpolarized structure function F_2^n got from NMC fits [53] are used to calculate g_2^{WW} in this proposal. The expected g_2^n statistical and systematic uncertainties, which are shown in Fig. 4.2 at 8.8 GeV and Fig. 4.3 at 11 GeV respectively, are the absolute errors.

The Expected matrix element d_2 with world data are shown in Fig. 4.4 with trigger prescale factor 10. Since we used g_2^{WW} (the twist-2 contribution) in the projections, the d_2 integral is always 0, and thus only the error bars in Fig. 4.4 are meaningful. Both statistical and systematic uncertainties from the cross section difference measurements are propagated into the projections, with a trigger prescale factor of 10 and 2. For a conservative estimate, the systematic uncertainties propagated from the cross sections and asymmetries are assumed fully correlated. In addition, we required $x_{min} > 0.40$ within the kinematic coverage to obtain the d_2 moments, and assigned 15% error for filling the unmeasured region. The x coverage requirement limits the d_2 projection to the region of $Q^2 < 6.5 \text{ GeV}$.

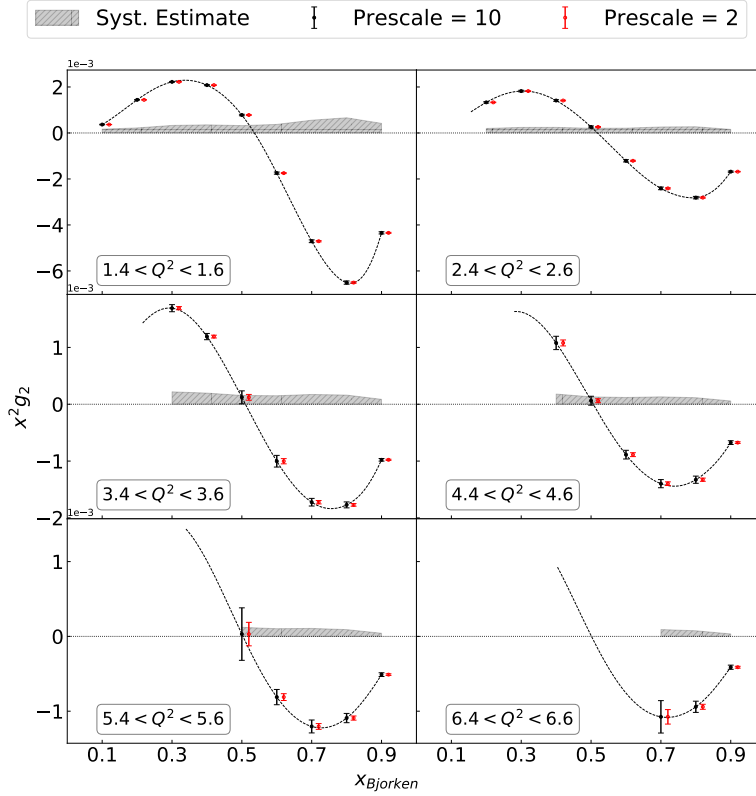


Figure 4.2: Expected $x^2 g_2^n$ versus x distribution at 8.8 GeV beam energy. Each subplot depicts the projections within a selected Q^2 bin. Error bars are statistical only, while systematic errors are shown with the gray shaded region. The black filled circles present the $x^2 g_2^n$ projection with a prescale factor “10”, and the red open dots, shifted horizontally, represent the projection with a prescale factor “2” (count for the random coincident trigger events).

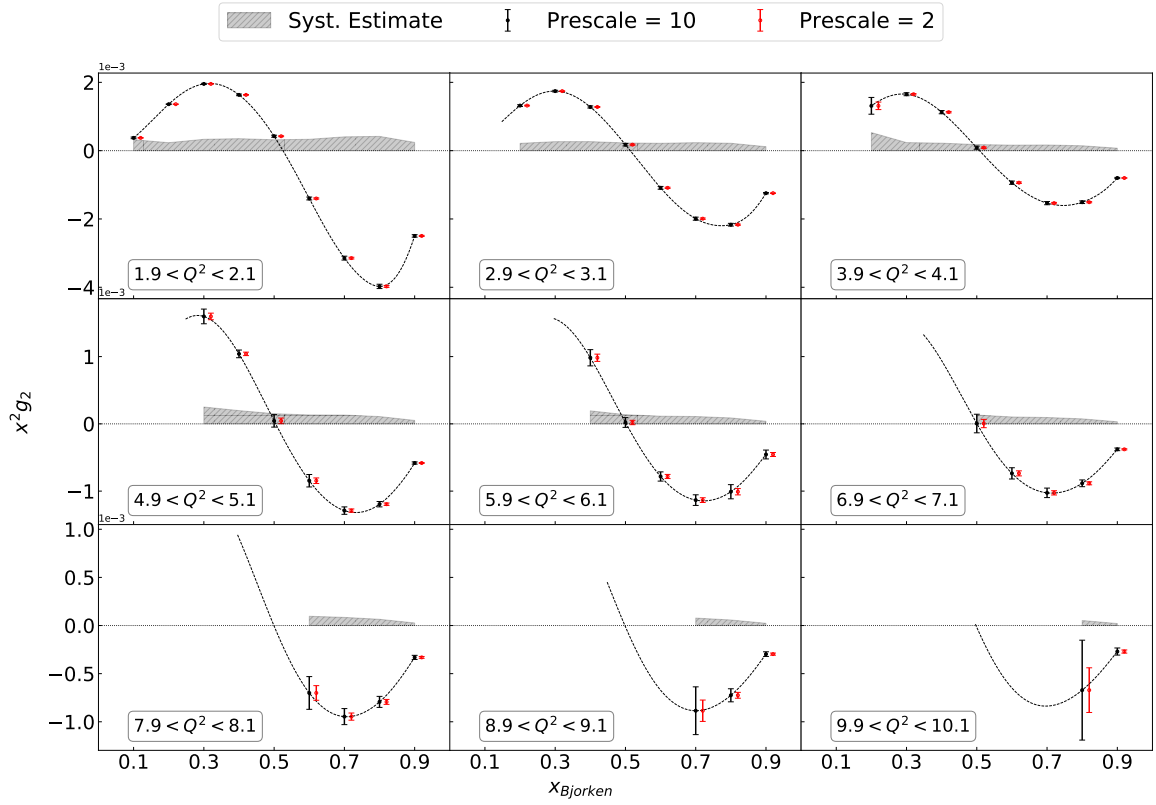


Figure 4.3: Expected $x^2 g_2^n$ versus x distribution at 11 GeV beam energy. Each subplot depicts the projections within a selected Q^2 bin. Error bars are statistical only, while systematic errors are shown with the gray shaded region. The black filled circles present the $x^2 g_2^n$ projection with a prescale factor “10”, and the red open dots, shifted horizontally, represent the projection with a prescale factor “2” (count for the random coincident trigger events).

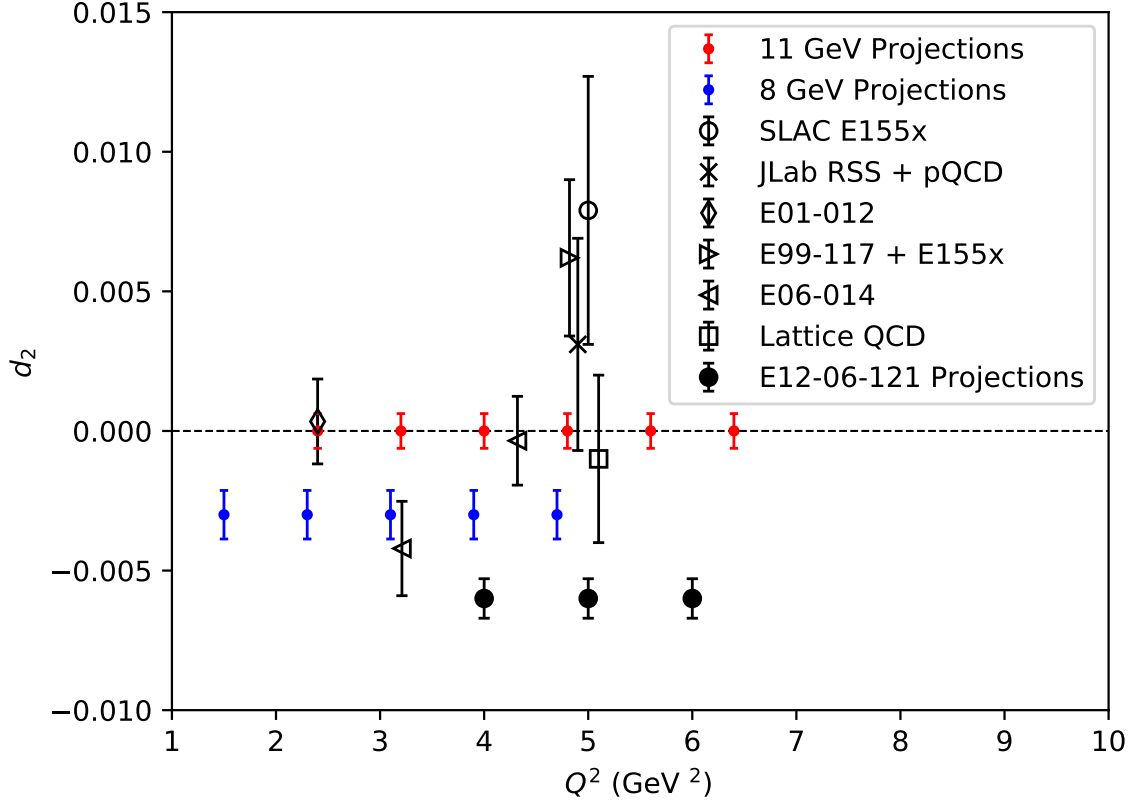


Figure 4.4: Expected results of d_2^n with trigger prescale factor “10” are shown by red points at 11 GeV and blue points at 8.8 GeV, respectively. The statistical and systematic uncertainties added in quadrature are shown as the error bars. The world data E155x [13], E99-117 and E155x [14], RSS [3], E06-014 [11], E01-012 [4], and the calculation of lattice QCD [9] at $Q^2 = 5 \text{ GeV}^2$ are presented with black open symbols, while the projections of E12-06-121 are marked as black solid dots. For a better visualization, the 8.8 GeV projections and E12-06-121 projections are manually shifted along the vertical axis, and the world data E155x, RSS+pQCD, and E99-117+E155x are shifted horizontally around $Q^2 = 5 \text{ GeV}^2$.

Chapter 5

Summary

In summary, we propose a run group project that runs simultaneously with E12-10-006 and E12-11-007. The experiment will take the free trigger space for the single electron triggers, and measure the inclusive cross section difference for doubly polarized e - ${}^3\text{He}$ scattering. The additional data from this measurement, combined with the longitudinally polarized ${}^3\text{He}$ data from E12-11-007, enable the precise extraction of $g_2^n(x, Q^2)$ at $1.5 < Q^2 < 10 \text{ GeV}^2$ and $x > 0.1$ and evaluate $d_2^n(Q^2)$ with $1.5 < Q^2 < 6.5 \text{ GeV}^2$. The experimental result not only measures the uncharted high x and high Q^2 region for $g_2^n(x, Q^2)$, but also provides an opportunity to better understand the moment $d_2^n(Q^2)$, and hence the associated quark-gluon correlations within the neutron.

References

- [1] P.L. Anthony et al. Precision measurement of the proton and deuteron spin structure functions g_2 and asymmetries a_2 . *Physics Letters B*, 553(1):18 – 24, 2003.
- [2] X. Zheng et al. Precision measurement of the neutron spin asymmetries and spin-dependent structure functions in the valence quark region. *Phys. Rev. C*, 70:065207, Dec 2004.
- [3] Frank R. Wesselmann et al. Proton spin structure in the resonance region. *Phys. Rev. Lett.*, 98:132003, 2007.
- [4] P. Solvignon et al. Moments of the neutron g_2 structure function at intermediate Q^2 . *Phys. Rev. C*, 92(1):015208, 2015.
- [5] E. Stein et al. QCD sum rule calculation of twist - three contributions to polarized nucleon structure functions. *Phys. Lett. B*, 343:369–376, 1995.
- [6] I.I. Balitsky et al. Power corrections $\frac{1}{Q^2}$ to parton sum rules for deep inelastic scattering from polarized targets. *Phys. Lett. B*, 242:245–250, 1990. [Erratum: *Phys.Lett.B* 318, 648 (1993)].
- [7] H. Weigel et al. Polarized nucleon structure functions within a chiral soliton model. *Phys. Rev. D*, 55:6910–6923, 1997.
- [8] X. Song. Polarized structure function g_2 in the c.m. bag model. *Phys. Rev. D*, 54:1955–1966, Aug 1996.
- [9] M. Gockeler et al. Investigation of the second moment of the nucleon’s $g(1)$ and $g(2)$ structure functions in two-flavor lattice QCD. *Phys. Rev. D*, 72:054507, 2005.
- [10] M. Posik et al. A Precision Measurement of the Neutron Twist-3 Matrix Element d_2^n : Probing Color Forces. *Phys. Rev. Lett.*, 113(2):022002, 2014.
- [11] D Flay et al. Measurements of d_2^n and a_1^n : Probing the neutron spin structure. *Physical Review D*, 94(5):052003, 2016.
- [12] W Armstrong, , et al. Revealing color forces with transverse polarized electron scattering. *Physical review letters*, 122(2):022002, 2019.
- [13] PL Anthony et al. Measurement of the proton and deuteron spin structure functions g_2 and asymmetry a_2 . *Physics Letters B*, 458(4):529–535, 1999.
- [14] X. Zheng et al. Precision measurement of the neutron spin asymmetries and spin-dependent structure functions in the valence quark region. *Phys. Rev. C*, 70:065207, 2004.
- [15] A.I. Signal. Calculations of higher twist distribution functions in the MIT bag model. *Nucl. Phys. B*, 497:415–434, 1997.

- [16] V.M. Braun, T. Lautenschlager, A.N. Manashov, and B. Pirnay. Higher twist parton distributions from light-cone wave functions. *Phys. Rev. D*, 83:094023, 2011.
- [17] S.E. Kuhn et al. Spin Structure of the Nucleon - Status and Recent Results. *Prog. Part. Nucl. Phys.*, 63:1–50, 2009.
- [18] S. Wandzura et al. Sum rules for spin-dependent electroproduction- test of relativistic constituent quarks. *Physics Letters B*, 72(2):195 – 198, 1977.
- [19] B. Adeva et al. Spin asymmetries A_1 and structure functions g_1 of the proton and the deuteron from polarized high energy muon scattering. *Phys. Rev. D*, 58:112001, 1998.
- [20] K. Abe et al. Measurements of the proton and deuteron spin structure functions g_1 and g_2 . *Phys. Rev. D*, 58:112003, Oct 1998.
- [21] Kenneth G. Wilson et al. Non-lagrangian models of current algebra. *Phys. Rev.*, 179:1499–1512, Mar 1969.
- [22] B.W. Filippone and Xiang-Dong Ji. The Spin structure of the nucleon. *Adv. Nucl. Phys.*, 26:1, 2001.
- [23] Matthias Burkardt. Transverse force on quarks in deep-inelastic scattering. *Phys. Rev. D*, 88:114502, Dec 2013.
- [24] M Göckeler et al. Investigation of the second moment of the nucleon’s g_1 and g_2 structure functions in two-flavor lattice qcd. *Physical Review D*, 72(5):054507, 2005.
- [25] Xiangdon Ji. The nucleon structure functions from deep-inelastic scattering with electroweak currents. *Nuclear Physics B*, 402(1):217 – 250, 1993.
- [26] E.V. Shuryak and A.I. Vainshtein. Theory of power corrections to deep inelastic scattering in quantum chromodynamics (i). q^2 effects. *Nuclear Physics B*, 199(3):451 – 481, 1982.
- [27] Hugh Burkhardt et al. Sum rules for forward virtual compton scattering. *Annals of Physics*, 56(2):453 – 463, 1970.
- [28] Jian-Ping Chen. Moments of spin structure functions: Sum rules and polarizabilities. *International Journal of Modern Physics E*, 19(10), 10 2010.
- [29] Airapetian et al. Measurement of the virtual-photon asymmetry a_2 and the spin-structure function g_2 of the proton. *The European Physical Journal C*, 72(3):1921, 2012.
- [30] M. Amarian et al. Q^2 evolution of the neutron spin structure moments using a ^3He target. *Phys. Rev. Lett.*, 92:022301, Jan 2004.
- [31] K. Kramer et al. Q^2 dependence of the neutron spin structure function g_2^n at low Q^2 . *Phys. Rev. Lett.*, 95:142002, Sep 2005.
- [32] V. Sulkosky et al. Measurement of the ^3he spin-structure functions and of neutron (^3he) spin-dependent sum rules at $0.035 < q^2 < 0.24 \text{ geV}^2$. *Physics Letters B*, 805:135428, 2020.
- [33] Chao Gu. The spin structure of the proton at low q^2 a measurement of the structure function g_p^2 . Technical report, Thomas Jefferson National Accelerator Facility, Newport News, VA (United States), 2016.
- [34] P. Solvignon et al. Quark-Hadron Duality in Neutron (He-3) Spin Structure. *Phys. Rev. Lett.*, 101:182502, 2008.

- [35] J.P. Chen et al. Target Single Spin Asymmetry in Semi-Inclusive Deep-Inelastic ($e, e\pi^\pm$) Reaction on a Transversely Polarized ^3He Target at 8.8 and 11 GeV, https://www.jlab.org/exp_prog/PACpage/PAC38/proposals/Previously_Approved/E12-10-006-update.pdf.
- [36] SoLID Collaboration. Transversely Polarized Proton Target, https://www.jlab.org/exp_prog/proposals/11/PR12-11-108.pdf.
- [37] X. Qian et al. Single spin asymmetries in charged pion production from semi-inclusive deep inelastic scattering on a transversely polarized ^3He target at $Q^2 = 1.4 - 2.7\text{GeV}^2$. *Phys. Rev. Lett.*, 107:072003, Aug 2011.
- [38] J. Zhang et al. Dihadron Electroproduction in DIS with Transversely Polarized ^3He Target at 11 and 8.8 GeV, https://www.jlab.org/exp_prog/proposals/14/E12-10-006A.pdf.
- [39] G.M. Huber et al. Measurement of Deep Exclusive π^- Production using a Transversely Polarized ^3He Target and the SoLID Spectrometer, https://www.jlab.org/exp_prog/proposals/17/E12-10-006B.pdf.
- [40] Zhihong Ye. Personal communications.
- [41] Ye Tian. Phd thesis draft.
- [42] J.P. Chen et al. Asymmetries in Semi-Inclusive Deep-Inelastic ($e, e'\pi^\pm$ reactions on a Longitudinally Polarized ^3He Target at 8.8 and 11 GeV), https://www.jlab.org/exp_prog/PACpage/PAC38/proposals/Previously_Approved/E12-11-007_Update.pdf.
- [43] I V Akushevich and N M Shumeiko. Radiative effects in deep inelastic scattering of polarized leptons by polarized light nuclei. *Journal of Physics G: Nuclear and Particle Physics*, 20(4):513–530, apr 1994.
- [44] Yung-Su Tsai. Pair production and bremsstrahlung of charged leptons. *Rev. Mod. Phys.*, 46:815–851, Oct 1974.
- [45] SoLID Collaboration. SoLID Updated Preliminary Conceptual Design Report, <https://hallaweb.jlab.org/12GeV/SoLID/files/solid-precdr-Nov2019.pdf>.
- [46] S. Agostinelli et al. Geant4 simulation toolkit. *Nuclear Instruments and Methods in Physics Research Section A: Accelerators, Spectrometers, Detectors and Associated Equipment*, 506(3):250 – 303, 2003.
- [47] R.-W. Schulze and P. U. Sauer. Inelastic electron scattering from the three-nucleon bound states with polarization. *Phys. Rev. C*, 48:38–63, Jul 1993.
- [48] A. Kievsky, E. Pace, G. Salmè, and M. Viviani. Neutron electromagnetic form factors and inclusive scattering of polarized electrons by polarized ^3He and ^3H targets. *Phys. Rev. C*, 56:64–75, Jul 1997.
- [49] J. J. Ethier and W. Melnitchouk. Comparative study of nuclear effects in polarized electron scattering from ^3He . *Phys. Rev. C*, 88:054001, Nov 2013.
- [50] P. H. Solvignon. *Measurement of the ^3He Spin Structure Functions in the Resonance Region: A Test of Quark-Hadron Duality on the Neutron*. PhD thesis, Temple University, 2006.

- [51] Andy Buckley et al. LHAPDF6: parton density access in the LHC precision era. *Eur. Phys. J. C*, 75:132, 2015.
- [52] PL Anthony, RG Arnold, T Averett, HR Band, MC Berisso, H Borel, PE Bosted, Stephen L Bultmann, M Buenerd, T Chupp, et al. Measurements of the q^2 -dependence of the proton and neutron spin structure functions g_{1p} and g_{1n} . *Physics Letters B*, 493(1-2):19–28, 2000.
- [53] M. Arneodo et al. Measurement of the proton and the deuteron structure functions, $F_2(p)$ and $F_2(d)$. *Phys. Lett. B*, 364:107–115, 1995.